J Toxicol Pathol 2025; 38: 167–175

Original Article

Novel three-dimensional analysis method for accurate evaluation of cutaneous small sensory nerve fibers in mice

Minori Inanaga-Kojima[1], Tetsuro Matsuura[1] and Kiyokazu Ozaki[1*]

[1] Laboratory of Pathology, Faculty of Pharmaceutical Science, Setsunan University, 45-1 Nagaotohge-cho, Hirakata, Osaka 573-0101, Japan

Abstract: Intraepidermal nerve fiber (IENF) density is commonly evaluated to diagnose peripheral neuropathy. However, conventional two-dimensional (2D) analysis using rodent models shows high interstudy variability. Three-dimensional (3D) IENF analysis has been proposed for human skin biopsies because the spatial location of each nerve can be easily determined. However, no studies have compared 2D and 3D analyses of mouse cutaneous nerve fibers under the same conditions. We aimed to establish a more accurate analysis method for mouse cutaneous nerve fibers. We used the glabrous plantar metatarsal skin of male C57BL/6J mice. The middle area of the plantar skin was used for 2D and 3D analyses, and the marginal area was also investigated in the 3D analysis. Tissue transparency, nerve fiber-specific antibodies, confocal microscopy, and IMARIS software were used for the 3D analysis. The 3D analysis clearly defined branching points and continuity, allowing accurate IENF density measurement. Conversely, the 2D analysis could not accurately determine IENF density because it could not detect the continuity of the nerve from the dermis to epidermis. Thus, the actual IENF density from the 3D analysis was significantly less than that from the 2D analysis. In addition, the density and length of IENFs in the middle area were significantly higher than those in the marginal area. This 3D approach enables the precise capture of IENF trajectories with various parameters, establishing a standard method for evaluating peripheral neuropathy models. Furthermore, our findings indicate that comparative studies aiming to analyze mouse IENF need to consider the site of skin sampling. (DOI: 10.1293/tox.2024-0085; J Toxicol Pathol 2025; 38: 167–175)

Key words: intraepidermal nerve fiber density, experimental animals, three-dimensional quantification method, tissue transparency technique, immunofluorescence staining

Introduction

Small sensory nerve fibers consist of myelinated A-delta and unmyelinated C-fibers, and selective impairment of these fibers is called small fiber sensory neuropathy[1, 2]. In human patients, small fiber sensory neuropathy is commonly diagnosed in metabolic diseases, such as diabetes and obesity, and can be a side effect of chemotherapy for advanced stage cancer[3–5]. The neuropathy in these diseases is called the "dying back type", in which axons degenerate from the ends of the nerve fibers[6–8]. Intraepidermal nerve fibers (IENFs) are susceptible to small fiber sensory neuropathy, and quantification of IENF density using skin biopsy of the distal leg is considered the most sensitive and specific diagnostic method in humans[9–11]. Currently, the guidelines proposed by the European Society of Neurology are used to measure the IENF density in numerous clinical trials related to peripheral neuropathies[12, 13]. Similarly, the IENF density is frequently measured as a marker of neuropathy in preclinical studies using rodents to elucidate the pathophysiology of peripheral neuropathy and develop therapeutic agents[14, 15]. Unlike human studies, rodent studies predominantly use glabrous plantar metatarsal skin for convenience, and sagittal sections of the middle area of the skin are commonly used in such studies[14, 16–25]. However, there are no standardized methods for measuring IENF density in studies using rodent models. The exact anatomical location of the skin to be sampled, the processing methods, and the image size used for analysis vary among studies, resulting in wide variability in quantitative IENF density results[21, 22, 26]. In fact, nerve fibers in the skin have a three-dimensional (3D) structure, running horizontally in a mesh pattern just below the epidermis and extending vertically within the epidermis[27, 28]. Therefore, the conventional two-dimensional (2D) analysis method using tissue sections has limitations in analytical accuracy, and a new method for more precise quantification is needed. To address this issue, a 3D analysis method for IENF density using skin biopsies has been proposed in humans, and its usefulness has been

Received: 4 October 2024, Accepted: 19 December 2024
Published online in J-STAGE: 2 January 2025
*Corresponding author: K Ozaki
(e-mail: ozaki@pharm.setsunan.ac.jp)
(Supplementary material: refer to J-STAGE https://www.jstage.jst.go.jp/browse/tox/list/-char/en)

demonstrated[29–31]. However, a 3D analysis of cutaneous nerve fibers, including the measurement of IENF density, has not yet been performed in rodent models. Thus, a comparative analysis of mouse cutaneous nerve fibers between 2D and 3D analyses under the same conditions would reveal both quantitative and morphological differences in methodology. The purpose of this study was to establish a 3D analysis method for more accurate qualitative and quantitative evaluation and to identify the issues with conventional 2D analysis that caused data variation in previous studies. In addition, differences in the density and length of nerve fibers depending on the location on the skin were analyzed using the 3D analysis.

Materials and Methods

Animals

Breeding conditions

Male C57BL/6J mice, provided by Jackson Laboratory Japan, were housed in TPX cages under a 12-:12-h light/dark cycle, 40–70% relative humidity, and 20–26°C temperature. Ventilation was provided by filtered fresh air; the mice had access to tap water and food *ad libitum*. Animal experiments were performed according to the ARRIVE guidelines[32] and approved by the Animal Care and Use Committee of Setsunan University (approval number: K23-20). All experiments were carried out in accordance with the relevant guidelines and regulations.

Reasons for male mouse selection

This study aimed to acquire normal IENF density data to assess small fiber sensory neuropathy in metabolic diseases such as diabetes using a mouse model. In patients with diabetes, peripheral neuropathy is more prevalent in male individuals than in female individuals[33, 34]. Therefore, most diabetic peripheral neuropathy models are based on male mice[20, 23–27, 35–41]. Male diabetic mice have been observed to exhibit more pronounced reductions in IENFD than female diabetic mice[42]. Thus, normal male mice were selected for this study.

Tissue preparation

Mice were obtained at eight weeks of age. After a week of acclimatization, the mice were euthanized after having undergone carbon dioxide exposure using a gradual-fill method. After euthanasia, the left and right glabrous plantar metatarsal skin was carefully incised. The left and right plantar regions were used for the 2D and 3D analyses, respectively. Five animals were used for each analysis. The mouse plantar metatarsal skin used in this study differs anatomically from the standard human sampling site, typically located 10 cm above the lateral malleolus, as described in previous studies[12, 13]. However, most rodent studies use skin from the plantar region to evaluate IENF density owing to the lack of hair in this region[14, 16–25]. In this study, we similarly utilized the plantar region skin to facilitate comparison with conventional analytical methods. Additionally, given its application to disease models such as diabetes, the plantar region of the foot, where the longest sensory nerve fibers are distributed, was deemed the optimal site for assessing length-dependent dying back degeneration[10, 43].

Frozen section immunofluorescent staining for 2D analysis (Fig. 1a)

The skin of the glabrous metatarsal area of the plantar region was cut and fixed in Zamboni solution at 4°C for 6 h while attached to filter paper. The skin was washed with 20% sucrose solution, immersed overnight at 4°C. Thereafter, the skin was incised in the mid-sagittal plane and then frozen and sectioned to a thickness of 75 µm. Three randomly selected sections were immersed in rabbit anti-PGP9.5 antibody (1:100; monoclonal antibody, ab108986; Abcam, Cambridge, UK) overnight at 4°C. Subsequently, the sections were immersed overnight at 4°C in a cocktail of goat anti-rabbit IgG conjugated with Alexa Fluor 594 (1:200; polyclonal antibody, A11037; Thermo Fisher Scientific, Waltham, MA, USA) as the secondary antibody and mouse anti-pan cytokeratin antibody conjugated with Alexa Fluor 488 (1:100; monoclonal antibody, 53-9003; Thermo Fisher Scientific). Images were captured at five areas using a confocal microscope (LSM 900; Carl Zeiss, Jena, Germany) with a Plan-Apochromat 10×/0.45 objective, and approximately 30 serial optical sections were analyzed at 1-µm intervals using appropriate software (ZEN; Carl Zeiss). Quantification of IENF density was performed on a projection image based on a stack of 30 serial optical sections. As the IENFs per mm of epidermis were calculated from a projection image, the actual analysis area of the counted IENFs was 0.03 mm^2 (Supplementary Fig. 1). Only fibers penetrating the epidermis were counted. IENFs per millimeter of epidermis were calculated by dividing the number of IENFs by the length of the epidermis.

Whole-mount immunofluorescent staining for 3D analysis (Fig. 1b)

The skin of the glabrous metatarsal area of the plantar region was cut and fixed with 4% paraformaldehyde (0.1 M TBS) overnight while attached to filter paper. The fixed skin was washed with TBS for 8 h at 4°C and then blocked with normal goat serum for 12 h at 37°C. The skin was then immersed in rabbit anti-beta III tubulin antibody (1:200; polyclonal antibody, ab18207; Abcam) for 3 days at 37°C, washed with TBS for 8 h at 4°C, and immersed for 5 days at 37°C in a cocktail of goat anti-rabbit IgG conjugated with Alexa Fluor 594 (1:200; polyclonal antibody, A11037; Thermo Fisher Scientific) as the secondary antibody and mouse anti-pan-cytokeratin antibody conjugated with Alexa Fluor 488 (1:50; monoclonal antibody, 53-9003; Thermo Fisher Scientific). Although anti-beta III tubulin antibody, employed as a neuronal marker in the 3D analysis, differs from the 2D analysis marker (anti-PGP9.5 antibody), both are pan-neuronal markers that exhibit the same immunoreactivity (Supplementary Fig. 2)[44]. The samples were then washed with TBS for 8 h at 4°C and immersed in a transparency reagent (LUCID-B, Photon Tech Innovations, Tokyo,

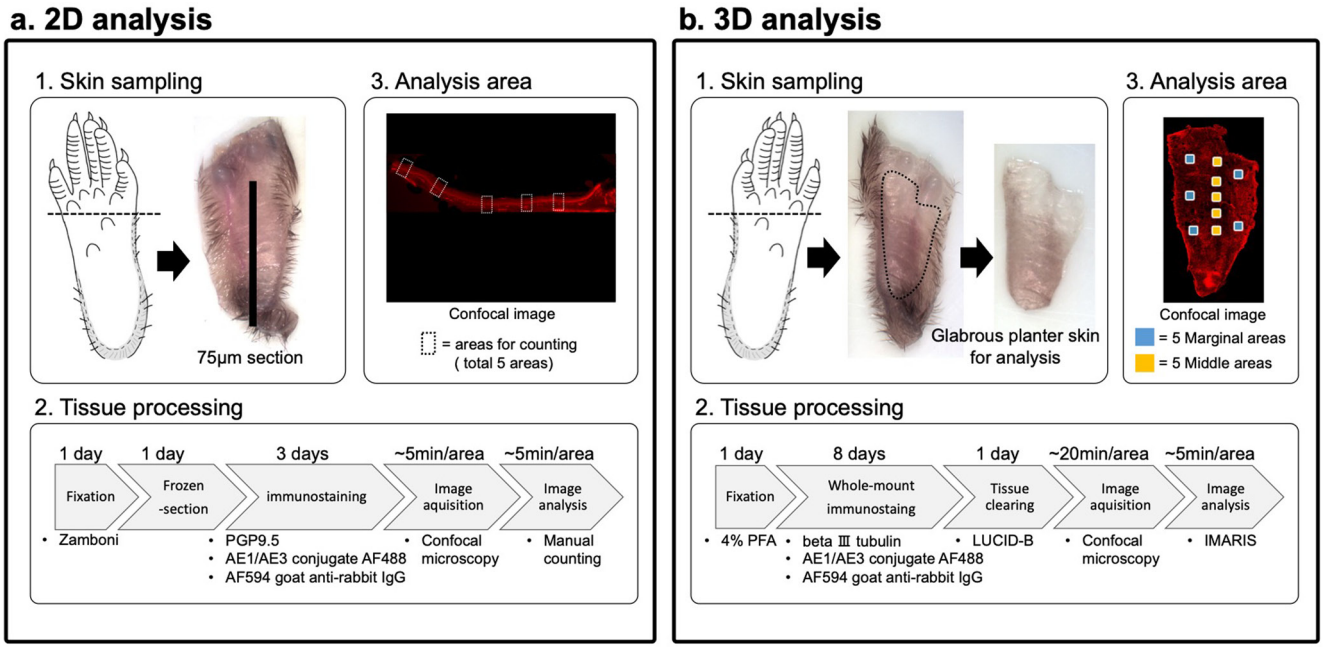

Fig. 1. Comparison of overall tissue processing for 2D and 3D analyses. (a) Overall tissue processing for 2D analysis. 1. Skin sampling site. The black line is the excision line of the plantar glabrous metatarsal region of the skin. 2. Outline of the steps from skin fixation to image analysis. 3. Analysis areas of the glabrous metatarsal region of the plantar skin. The image shows the whole section tiled after confocal imaging. The five dotted squares were analyzed. (b) Overall tissue processing for 3D analysis. 1. Skin sampling site. The dotted line is the excision area of the plantar glabrous metatarsal region of the skin. 2. Outline of the steps from skin fixation to image analysis. 3. Analysis areas of the glabrous metatarsal region of the plantar skin. The image shows the whole skin tiled after confocal imaging. In the analysis, the five blue squares were classified as the marginal area and the five yellow squares as the middle area. PFA, paraformaldehyde.

Japan) overnight at 37°C. Fluorescent-labeled cutaneous nerve fibers were z-stacked at 0.27-μm intervals with an XY plane of 512 × 512 pixels using a confocal microscope (LSM 900; Carl Zeiss) equipped with objective plan-apochromat 40×/1.4 oil DIC. All 3D images were acquired using 1× zoom at a frame time of 633.02 ms, with an XY plane of approximately 160 μm^2 and a height of approximately 40–50 μm (from the dermis to the granular layer). A total of 10 volume images were captured continuously at five locations, ranging from the middle to the marginal area of the glabrous metatarsal region of the plantar skin, to observe the nerve fibers passing through the epidermis and dermis. The number of IENFs per 0.03 mm^2 (the actual area of epidermis analyzed in the 2D analysis) was calculated in the 3D analysis to quantify the IENF density for comparison between the 2D and 3D analyses (Supplementary Fig. 1). For the quantitative analysis of cutaneous nerve fibers using 3D images, volume rendering was performed using the IMARIS software (Imaris 9.7; Bitplane, Belfast, UK). The nerve plexus running in the dermis was automatically reconstructed using the "filament tracer" function and the algorithm created by defining a threshold from the luminance values in the image, and then only nerve fibers running just below the epidermis were extracted. The nerve fibers that were unnecessary due to noise were manually reworked. The nerve fibers penetrating the epidermis were also reconstructed by semi-automatically tracking only those fibers penetrating the fluorescent signal area (epidermal area) of Alexa Fluor 488 using the "filament autopath" function by a certain fluorescence intensity threshold. IENFs that lost connection to the dermal nerve fibers were excluded from the quantitative analysis. The total length of nerve fibers in the dermis, the individual lengths of nerve fibers in the epidermis, the total length, and the presence of branching were quantitatively analyzed. The IENF density was calculated per mm^2 of epidermal area and per mm of dermal nerve fiber length. The number of IENFs per 0.03 mm^2 of epidermal area was also calculated for comparison with the IENF density obtained from the 2D and 3D analyses (Supplementary Fig. 1).

Statistics

Data are presented as mean ± standard deviation. The Wilcoxon test was used to compare the means between the groups. Differences were considered statistically significant at $p<0.05$. Statistical analysis was performed using JMP Pro 17 software (SAS Institute Japan, Tokyo, Japan).

Results

3D analysis using tissue transparency technology reveals the 3D structure of IENFs of the glabrous plantar metatarsal skin in mice

In the conventional 2D analysis, the dermal nerve fibers extending horizontally and the IENFs running verti-

cally in the glabrous plantar metatarsal skin were visualized using confocal microscopy (Fig. 2a). However, the IENFs overlapped the dermal nerve fibers that extended horizontally just below the epidermis because the 2D image was reconstructed into a projection image by overlapping the z-stack images. Thus, it was difficult to determine exactly which IENFs were connected to the dermal nerve fibers at the epidermis–dermis border (Fig. 2a). Meanwhile, 3D structural imaging revealed that nerve trunks consisting of several large nerve fibers penetrated just below the epidermis, branched, and fused to form a complex meshwork of nerve fibers in the dermis (Fig. 2b). In addition, the IENFs branched from the nerve fiber meshwork in the dermis and then extended spirally and vertically within the epidermis (Fig. 2c). After penetrating the epidermis, the IENFs scarcely branched, with approximately half (50.3 ± 16.2%) randomly disconnecting in the basal to granular layers (Fig. 2d). Comparing the IENF density between the 2D and 3D analyses over the same area (Supplementary Fig. 1), the density in the 2D analysis was 47.8 ± 9.0 fibers/0.03 mm^2, whereas that in the 3D analysis was 15.0 ± 7.6 fibers/0.03 mm^2. Thus, for the same epidermal area, the IENF density in the 3D analysis was approximately one-third of that in the 2D analysis ($p<0.0001$, Fig. 2e).

3D analysis of cutaneous nerve fibers using IMARIS software provides more accurate quantitative information than conventional 2D analysis

The IMARIS software reconstructed clear 3D images of the dermal nerve fibers and IENFs, providing more accurate quantitative data (Fig. 3a). The 3D analysis was able to capture the mesh network of the dermal nerve fibers and thus more accurately detect the branching points of IENFs from the dermal nerve fibers, resulting in the identification of the exact number of IENFs (Fig. 3a). The 3D analysis using IMARIS software not only quantified IENFs branching from the dermal nerves but also accurately measured the complicated trajectory of the nerve fibers (Fig. 3a, Supplementary Movie 1). As a result, in addition to measuring IENF density per epidermal area (mean: 500.8 ± 253.1 fibers/mm^2), accurate measurements could be obtained for IENF density per dermal nerve length (mean: 8.7 ± 4.2 fibers/mm), length of a single IENF (mean: 17.7 ± 4.8 μm), total length of IENFs (mean: 234.7 ± 153.7 μm), and total length of dermal nerve fibers (mean: 1,486.9 ± 330.6 μm) (Fig. 3b).

IENFs have different characteristics depending on the location of the glabrous plantar metatarsal skin

The qualitative and quantitative 3D analysis method we developed revealed site-specific differences in the number and length of IENFs (Fig. 4a and 4b). The mean values related to the IENFs in the margin versus the middle areas were as follows: 424.8 ± 236.1 vs. 576.8 ± 251.0 fibers/mm^2 (IENF density per epidermal area, $p=0.0309$, Fig. 4c), 7.0 ± 3.6 vs. 10.3 ± 4.2 fibers/mm (IENF density per dermal nerve length, $p=0.0062$, Fig. 4d), 15.2 ± 4.5 vs. 20.1 ± 3.8 mm (the length of a single IENF, $p=0.0002$, Fig. 4e), and 173.0 ± 103.4 vs. 296.4 ± 137.8 mm (the total length of IENFs, $p=0.0018$, Fig. 4f). For all the four parameters, the mean values in the middle area were significantly higher than those in the marginal area. Only the frequency of fragmented IENFs was significantly higher in the marginal area (55.9 ± 18.2%) than in the middle area (44.7 ± 11.9%, $p=0.0406$, Fig. 4h). On the contrary, the total length of dermal nerve fibers was 1,553.7 ± 342.3 mm in the marginal area and 1,420.2 ± 310.9 mm in the middle area, with no significant difference between the two locations ($p=0.1206$, Fig. 4g).

Discussion

This study clearly demonstrated the difference between the 2D and 3D analyses of nerve fibers throughout the glabrous plantar metatarsal skin in mice. The conventional 2D analysis usually uses a single projection image from multiple z-stack images of the vertical plane of the skin. Therefore, determining the exact continuity between horizontally extending dermal nerve fibers and vertically branching IENFs from a single projection image was difficult. In contrast, the 3D analysis accurately detected the branching points of the IENFs from the dermal nerve fibers and clarified that approximately half of the IENFs were randomly disconnected in the epidermis. Consequently, the IENF density in the 2D analysis was considerably higher than that in the 3D analysis when evaluated across equivalent epidermal areas. This finding suggests that the 2D images may have contained inaccurate data on IENFs that should not have been counted. Thus, these erroneous measurements may be responsible for the interstudy variability in IENF density observed in previous 2D analyses of mice, in addition to the lack of standardized methods[21, 22, 26]. To date, the difficulty in achieving transparency in the epidermis and capturing small-sized nerve fibers has prevented the establishment of a reliable method for 3D quantitative analysis for IENFs[21, 27, 45]. The method developed in this study effectively reproduced the 3D nerve distribution in mice, allowing the software to semi-automatically detect the exact location of nerve branches. As a result, we established a new 3D analysis method that can accurately identify IENFs both quantitatively and qualitatively.

Our 3D analysis method facilitated the accurate measurement of not only the number of IENFs but also the length of IENFs and dermal nerve fibers in mice. These new parameters provide a more comprehensive nerve fiber data-set to evaluate. In addition, the quantitative analysis revealed site-specific differences in both the density and length of IENFs. For all parameters of IENF density and the length of IENFs within the glabrous plantar epidermis, the mean values for the middle area were significantly higher than those for the marginal area. This discrepancy between skin sites may have contributed to the variation in IENF density observed in previous studies[21, 22, 26] using conventional 2D analysis. However, the exact reason for the higher IENF density in the middle area remains unknown and should be

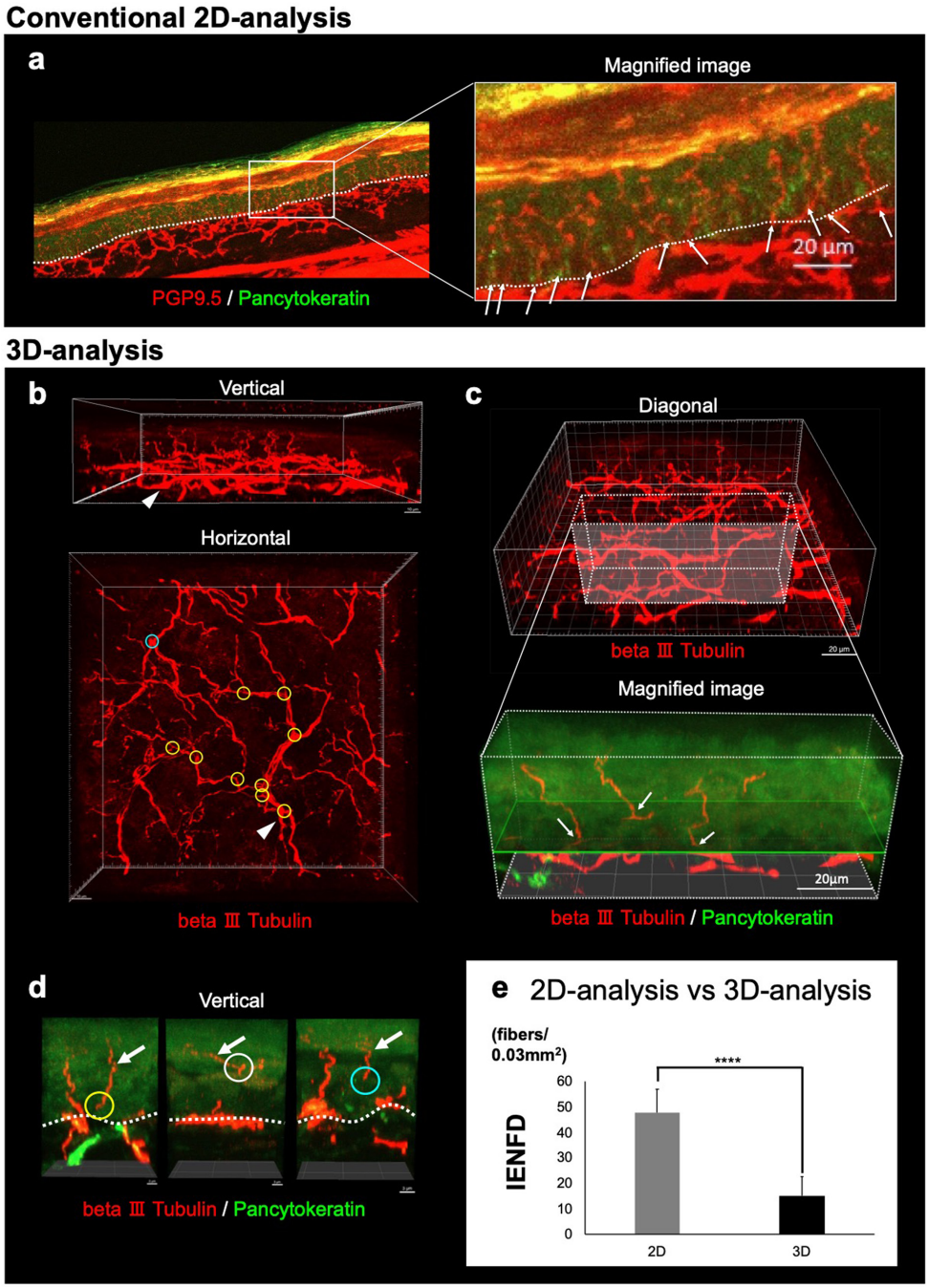

Fig. 2. Comparison of confocal images between the 2D and 3D analyses. (a) 2D analysis image. Red indicates nerve fibers labeled with PGP9.5 and green indicates epidermis labeled with pan-cytokeratin. Confocal image of a longitudinal cutaneous section with maximum intensity projection. The white dotted line indicates the length of the epidermis used to calculate the IENF density. In the magnified image of the white line square area, the white arrow indicates the IENFs to be counted. (b–d) 3D analysis image. Red indicates nerve fibers labeled with beta III-tubulin and green indicates epidermis labeled with pan-cytokeratin. (b) Vertical and horizontal images show nerve trunk penetration (white arrowheads), branching (yellow circles), and fusion (blue circle). (c) Diagonal images indicate the continuity of IENFs with dermal nerve fibers. In the magnified image of the white dotted line area in the diagonal image, the green framed plane indicates the boundary between the epidermis and dermis, and the white arrows indicate IENFs. (d) Some IENFs disconnect in the basal layer (yellow circle), granular layer (white circle), or between the layers (blue circle). (e) Comparison of IENF density between the 2D and 3D analyses for the same epidermal area. ****$p<0.0001$, Wilcoxon test. IENFD, intraepithelial nerve fiber density.

explored in future studies. One possible explanation is the difference in innervation, as the plantar region in mice is innervated by the tibial nerve in the middle area and the sural nerve in the marginal area[46]. This difference in innervation could account for the observed variation in IENF density.

Fragmented nerve fibers within the epidermis account-

a

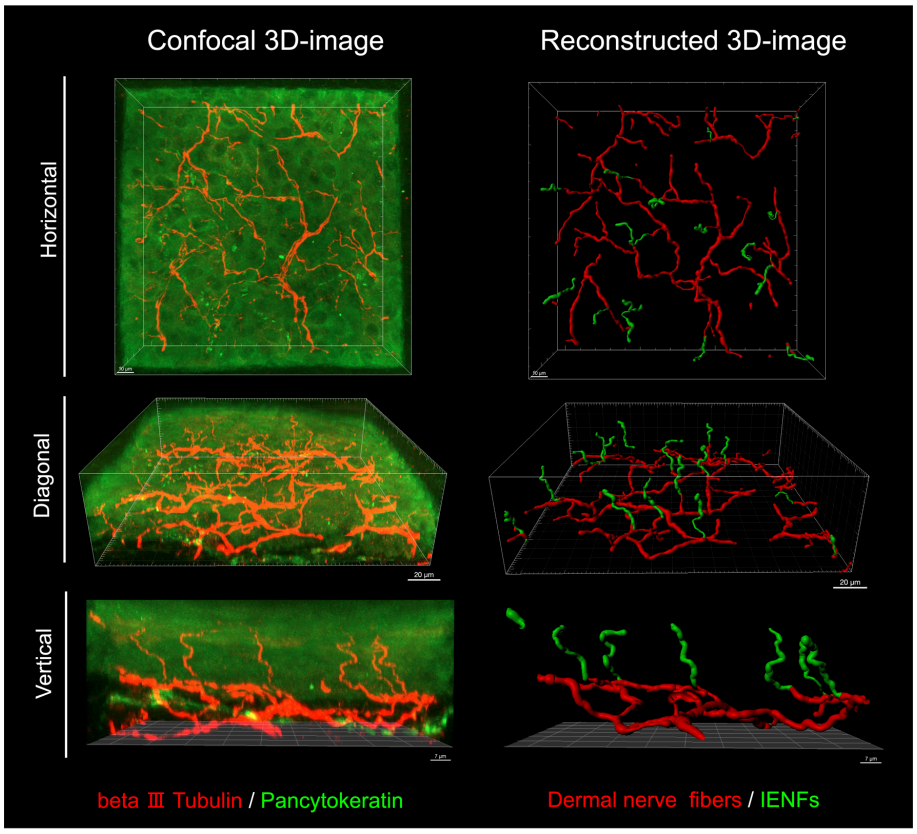

b

Measurement parameters	
IENFD per epidermal area (fibers/mm^2)	500.8 ± 253.1
IENFD per dermal nerve length (fibers/mm)	8.7 ± 4.2
Length of a single IENF(μm)	17.7 ± 4.8
Total length of the IENFs (μm)	234.7 ± 153.7
Total length of the dermal nerve fibers (μm)	1,486.9 ± 330.6

Fig. 3. Comparison of confocal and reconstructed 3D images of IENFs of the glabrous metatarsal region of the plantar skin. (a) Confocal and reconstructed 3D images. Red in the confocal images shows nerve fibers labeled with beta III-tubulin and green shows epidermal layers labeled with pan-cytokeratin. The reconstructed images show IENFs in green and dermal nerve fibers in red. (b) A list of parameters of cutaneous nerve fibers that can be measured using 3D analysis and the actual values measured in the glabrous metatarsal region of the plantar skin of five mice. IENF, intraepithelial nerve fiber; IENFD, intraepithelial nerve fiber density.

ed for approximately half of the nerve fibers observed within the epidermis, and their numbers were significantly higher in the marginal area than in the middle area. It is known that IENFs in mice extend into the granular layer[47]. Recent *in vivo* imaging of the skin has demonstrated that newly formed tight junctions in the granular cell layer prune and fragment IENFs, while IENFs are also fragmented in areas without tight junctions[45]. The fragmentation of IENFs is likely to affect their organization and density[45]. In the present study, IENF fragmentation was found in the granular cell layer as well as the basal cell layer near the basal lamina. This finding is consistent with previous reports[45, 47], suggesting that IENF fragmentation occurs randomly within the epidermis and is probably a physiological change related to epidermal cell turnover. Furthermore, in the present study, more fragmentation was observed in the marginal area, which may be related to the finding that IENF density was higher in the middle area and lower in the marginal area, indicating that the marginal area may be more prone to fragmentation.

The present study demonstrated that the majority of IENFs in the mouse plantar epidermis did not branch. In humans, IENFs exhibit substantial branching, especially in young individuals, and this structure simplifies with age, suggesting that the degree of nerve fiber branching may also be an indicator of neuropathy[29]. However, a limitation of this study is that in our young adult mice, the IENFs were sparsely branched, and the pattern was clearly different from that of humans. Thus, further studies are needed to

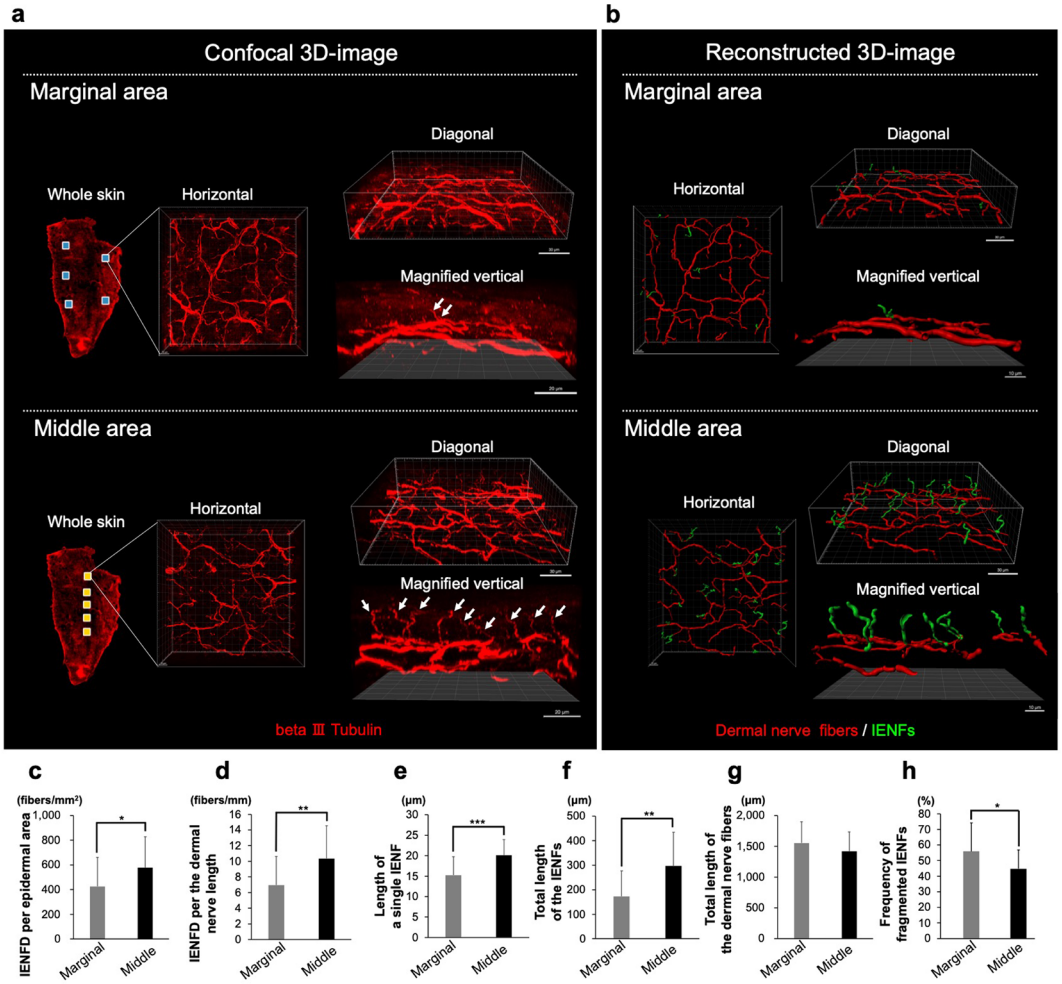

Fig. 4. Comparison of IENFs between the marginal and middle areas of the glabrous metatarsal region of the plantar skin. (a) Representative confocal 3D images of the marginal and middle areas of the glabrous metatarsal region of the plantar skin. The five blue squares on the whole skin represent the area analyzed as the marginal area and the five yellow squares represent the actual skin area analyzed as the middle area. White arrows in the magnified vertical image indicate IENFs. Red in the confocal images shows nerve fibers labeled with beta III-tubulin. (b) Representative reconstructed 3D images of the marginal and middle areas of the glabrous metatarsal region of the plantar skin. The reconstructed images show IENFs in green and dermal nerve fibers in red. (c–h) Results of quantitative analyses of cutaneous nerve fibers in the marginal and middle areas. (c) IENF density per epidermal area (fibers/mm^2). (d) IENF density per dermal nerve length (fibers/mm). (e) The length of a single IENF (mm). (f) The total length of IENFs (mm). (g) The total length of dermal nerve fibers (mm). (h) Frequency of fragmented IENFs (%). *p<0.05; **p<0.01; ***p<0.001, Wilcoxon test. IENF, intraepithelial nerve fiber; IENFD, intraepithelial nerve fiber density.

analyze the branching patterns of IENF with age in mice.

The newly developed 3D method enables straightforward and accurate morphological evaluation of peripheral neuropathy, minimizing measurement discrepancies between studies compared to the 2D method. In addition, achieving transparency in skin samples is straightforward, without the need to prepare genetically modified mice with fluorescent molecules knocked into their genes. This versatile method holds promise for application across various mouse disease models in future studies.

Disclosure of Potential Conflicts of Interest: The authors declare no conflicts of interest. The funding body had no involvement in the design of the study; collection, analysis, and interpretation of data; writing of the report; or the decision to publish the article.

Acknowledgments: We thank the laboratory staff and students of Setsunan University for their technical assistance.

References

1. Hovaguimian A, and Gibbons CH. Diagnosis and treatment of pain in small-fiber neuropathy. Curr Pain Headache Rep. **15**: 193–200. 2011. [Medline] [CrossRef]
2. Raasing LRM, Vogels OJM, Veltkamp M, van Swol CFP, and Grutters JC. Current view of diagnosing small fiber neuropathy. J Neuromuscul Dis. **8**: 185–207. 2021. [Med-

line] [CrossRef]
3. Feldman EL, Nave KA, Jensen TS, and Bennett DLH. New horizons in diabetic neuropathy: mechanisms, bioenergetics, and pain. Neuron. **93**: 1296–1313. 2017. [Medline] [CrossRef]
4. Timmins HC, Li T, Kiernan MC, Horvath LG, Goldstein D, and Park SB. Quantification of small fiber neuropathy in chemotherapy-treated patients. J Pain. **21**: 44–58. 2020. [Medline] [CrossRef]
5. Stino AM, and Smith AG. Peripheral neuropathy in prediabetes and the metabolic syndrome. J Diabetes Investig. **8**: 646–655. 2017. [Medline] [CrossRef]
6. Prior R, Van Helleputte L, Benoy V, and Van Den Bosch L. Defective axonal transport: a common pathological mechanism in inherited and acquired peripheral neuropathies. Neurobiol Dis. **105**: 300–320. 2017. [Medline] [CrossRef]
7. Schaumburg HH, Zotova E, Raine CS, Tar M, and Arezzo J. The rat caudal nerves: a model for experimental neuropathies. J Peripher Nerv Syst. **15**: 128–139. 2010. [Medline] [CrossRef]
8. Birnbaum J, and Bingham CO 3rd. Non-length-dependent and length-dependent small-fiber neuropathies associated with tumor necrosis factor (TNF)-inhibitor therapy in patients with rheumatoid arthritis: expanding the spectrum of neurological disease associated with TNF-inhibitors. Semin Arthritis Rheum. **43**: 638–647. 2014. [Medline] [CrossRef]
9. Myers MI, and Peltier AC. Uses of skin biopsy for sensory and autonomic nerve assessment. Curr Neurol Neurosci Rep. **13**: 323. 2013. [Medline] [CrossRef]
10. Nolano M, Tozza S, Caporaso G, and Provitera V. Contribution of skin biopsy in peripheral neuropathies. Brain Sci. **10**: 989. 2020. [Medline] [CrossRef]
11. McCarthy BG, Hsieh ST, Stocks A, Hauer P, Macko C, Cornblath DR, Griffin JW, and McArthur JC. Cutaneous innervation in sensory neuropathies: evaluation by skin biopsy. Neurology. **45**: 1848–1855. 1995. [Medline] [CrossRef]
12. Lauria G, Cornblath DR, Johansson O, McArthur JC, Mellgren SI, Nolano M, Rosenberg N, Sommer C. European Federation of Neurological Societies EFNS guidelines on the use of skin biopsy in the diagnosis of peripheral neuropathy. Eur J Neurol. **12**: 747–758. 2005. [Medline] [CrossRef]
13. Lauria G, Hsieh ST, Johansson O, Kennedy WR, Leger JM, Mellgren SI, Nolano M, Merkies IS, Polydefkis M, Smith AG, Sommer C, Valls-Solé J. European Federation of Neurological Societies Peripheral Nerve Society. European Federation of Neurological Societies/Peripheral Nerve Society Guideline on the use of skin biopsy in the diagnosis of small fiber neuropathy. Report of a joint task force of the European Federation of Neurological Societies and the Peripheral Nerve Society. Eur J Neurol. **17**: 903–912, e44–e49. 2010. [Medline] [CrossRef]
14. Thomas S, Enders J, Kaiser A, Rovenstine L, Heslop L, Hauser W, Chadwick A, and Wright D. Abnormal intraepidermal nerve fiber density in disease: a scoping review. Front Neurol. **14**: 1161077. 2023. [Medline] [CrossRef]
15. Mangus LM, Rao DB, and Ebenezer GJ. Intraepidermal nerve fiber analysis in human patients and animal models of peripheral neuropathy: a comparative review. Toxicol Pathol. **48**: 59–70. 2020. [Medline] [CrossRef]
16. Tian T, Li H, Zhang S, and Yang M. Characterization of sensory and motor dysfunction and morphological alterations in late stages of type 2 diabetic mice. Front Endocrinol (Lausanne). **15**: 1374689. 2024. [Medline] [CrossRef]
17. Lee D, Yoon E, Ham SJ, Lee K, Jang H, Woo D, Lee DH, Kim S, Choi S, and Chung J. Diabetic sensory neuropathy and insulin resistance are induced by loss of UCHL1 in Drosophila. Nat Commun. **15**: 468. 2024. [Medline] [CrossRef]
18. Handzlik MK, Gengatharan JM, Frizzi KE, McGregor GH, Martino C, Rahman G, Gonzalez A, Moreno AM, Green CR, Guernsey LS, Lin T, Tseng P, Ideguchi Y, Fallon RJ, Chaix A, Panda S, Mali P, Wallace M, Knight R, Gantner ML, Calcutt NA, and Metallo CM. Insulin-regulated serine and lipid metabolism drive peripheral neuropathy. Nature. **614**: 118–124. 2023. [Medline] [CrossRef]
19. Lv X, Mao Y, Cao S, and Feng Y. Animal models of chemotherapy-induced peripheral neuropathy for hematological malignancies: a review. Ibrain. **9**: 72–89. 2022. [Medline] [CrossRef]
20. Tseng KY, Wang HC, Wang YH, Su MP, Cheng KF, Cheng KI, and Chang LL. Peripheral nerve denervation in streptozotocin-induced diabetic rats is reduced by cilostazol. Medicina (Kaunas). **59**: 553. 2023. [Medline]
21. Daeschler SC, Zhang J, Gordon T, Borschel GH, and Feinberg K. Foretinib mitigates cutaneous nerve fiber loss in experimental diabetic neuropathy. Sci Rep. **12**: 8444. 2022. [Medline] [CrossRef]
22. Ezaka M, Marutani E, Miyazaki Y, Kanemaru E, Selig MK, Boerboom SL, Ostrom KF, Stemmer-Rachamimov A, Bloch DB, Brenner GJ, Ohshima E, and Ichinose F. Oral administration of glutathione trisulfide increases reactive sulfur levels in dorsal root ganglion and ameliorates paclitaxel-induced peripheral neuropathy in mice. Antioxidants. **11**: 2122. 2022. [Medline] [CrossRef]
23. Umbaugh DS, Maciejewski JC, Wooten JS, and Guilford BL. Neuronal inflammation is associated with changes in epidermal innervation in high fat fed mice. Front Physiol. **13**: 891550. 2022. [Medline] [CrossRef]
24. Hossain MJ, Kendig MD, Letton ME, Morris MJ, and Arnold R. Peripheral neuropathy phenotyping in rat models of type 2 diabetes mellitus: evaluating uptake of the Neurodiab guidelines and identifying future directions. Diabetes Metab J. **46**: 198–221. 2022. [Medline] [CrossRef]
25. Takahashi K, Mizukami H, Osonoi S, Ogasawara S, Hara Y, Kudoh K, Takeuchi Y, Sasaki T, Daimon M, and Yagihashi S. Inhibitory effects of xanthine oxidase inhibitor, topiroxostat, on development of neuropathy in db/db mice. Neurobiol Dis. **155**: 105392. 2021. [Medline] [CrossRef]
26. Shavit-Stein E, Gofrit SG, Gayster A, Teldan Y, Ron A, Abu Bandora E, Golderman V, Gera O, Harnof S, Chapman J, and Dori A. Treatment of diabetic neuropathy with a novel PAR1-targeting molecule. Biomolecules. **10**: 1552. 2020. [Medline] [CrossRef]
27. Yamazaki T, Li W, Yang L, Li P, Cao H, Motegi SI, Udey MC, Bernhard E, Nakamura T, and Mukouyama YS. Whole-mount adult ear skin imaging reveals defective neuro-vascular branching morphogenesis in obese and type 2 diabetic mouse models. Sci Rep. **8**: 430. 2018. [Medline] [CrossRef]
28. Wendelschafer-Crabb G, Kennedy WR, and Walk D. Morphological features of nerves in skin biopsies. J Neurol Sci. **242**: 15–21. 2006. [Medline] [CrossRef]
29. Kim DH, Lee SJ, Kim JH, Park SJ, Seo SH, Ahn HH, Sun

W, Kim BJ, and Rhyu IJ. Whole structural reconstruction and quantification of epidermal innervation through the suction blister method and skin-clearing technique. Sci Rep. **12**: 13596. 2022. [Medline] [CrossRef]
30. Tan Y, Ng WJ, Lee SZX, Lee BTK, Nattkemper LA, Yosipovitch G, Ng LG, and Tey HL. 3-dimensional optical clearing and imaging of pruritic atopic dermatitis and psoriasis skin reveals downregulation of epidermal innervation. J Invest Dermatol. **139**: 1201–1204. 2019. [Medline] [CrossRef]
31. Kim DH, Lee SJ, Lee E, Hong JH, Seo SH, Ahn HH, Kim B-J, Sun W, and Rhyu IJ. Tissue-clearing technique and cutaneous nerve biopsies: quantification of the intraepidermal nerve-fiber density using active clarity technique-pressure related efficient and stable transfer of macromolecules into organs. J Clin Neurol. **15**: 537–544. 2019. [Medline] [CrossRef]
32. Kilkenny C, Browne WJ, Cuthill IC, Emerson M, and Altman DG. Improving bioscience research reporting: the ARRIVE guidelines for reporting animal research. PLoS Biol. **8**: e1000412. 2010. [Medline] [CrossRef]
33. Aaberg ML, Burch DM, Hud ZR, and Zacharias MP. Gender differences in the onset of diabetic neuropathy. J Diabetes Complications. **22**: 83–87. 2008. [Medline] [CrossRef]
34. Abraham A, Barnett C, Katzberg HD, Lovblom LE, Perkins BA, and Bril V. Sex differences in neuropathic pain intensity in diabetes. J Neurol Sci. **388**: 103–106. 2018. [Medline] [CrossRef]
35. Sullivan KA, Hayes JM, Wiggin TD, Backus C, Su Oh S, Lentz SI, Brosius F 3rd, and Feldman EL. Mouse models of diabetic neuropathy. Neurobiol Dis. **28**: 276–285. 2007. [Medline] [CrossRef]
36. Kan M, Guo G, Singh B, Singh V, and Zochodne DW. Glucagon-like peptide 1, insulin, sensory neurons, and diabetic neuropathy. J Neuropathol Exp Neurol. **71**: 494–510. 2012. [Medline] [CrossRef]
37. O'Brien PD, Sakowski SA, and Feldman EL. Mouse models of diabetic neuropathy. ILAR J. **54**: 259–272. 2014. [Medline] [CrossRef]
38. Yorek MS, Obrosov A, Shevalye H, Holmes A, Harper MM, Kardon RH, and Yorek MA. Effect of diet-induced obesity or type 1 or type 2 diabetes on corneal nerves and peripheral neuropathy in C57Bl/6J mice. J Peripher Nerv Syst. **20**: 24–31. 2015. [Medline] [CrossRef]
39. Leckelt J, Guimarães P, Kott A, Ruggeri A, Stachs O, and Baltrusch S. Early detection of diabetic neuropathy by investigating CNFL and IENFD in thy1-YFP mice. J Endocrinol. **231**: 147–157. 2016. [Medline] [CrossRef]
40. Osonoi S, Mizukami H, Takeuchi Y, Sugawa H, Ogasawara S, Takaku S, Sasaki T, Kudoh K, Ito K, Sango K, Nagai R, Yamamoto Y, Daimon M, Yamamoto H, and Yagihashi S. RAGE activation in macrophages and development of experimental diabetic polyneuropathy. JCI Insight. **7**: e160555. 2022. [Medline] [CrossRef]
41. Nichols JM, Pham HV, Lee EF, Mahalingam R, and Shepherd AJ. Single-cell analysis of age-related changes in leukocytes of diabetic mouse hindpaws. Cell Mol Life Sci. **81**: 146. 2024. [Medline] [CrossRef]
42. O'Brien PD, Hur J, Robell NJ, Hayes JM, Sakowski SA, and Feldman EL. Gender-specific differences in diabetic neuropathy in BTBR ob/ob mice. J Diabetes Complications. **30**: 30–37. 2016. [Medline] [CrossRef]
43. Feldman EL, Callaghan BC, Pop-Busui R, Zochodne DW, Wright DE, Bennett DL, Bril V, Russell JW, and Viswanathan V. Diabetic neuropathy. Nat Rev Dis Primers. **5**: 41. 2019. [Medline] [CrossRef]
44. Lauria G, Borgna M, Morbin M, Lombardi R, Mazzoleni G, Sghirlanzoni A, and Pareyson D. Tubule and neurofilament immunoreactivity in human hairy skin: markers for intraepidermal nerve fibers. Muscle Nerve. **30**: 310–316. 2004. [Medline] [CrossRef]
45. Takahashi S, Ishida A, Kubo A, Kawasaki H, Ochiai S, Nakayama M, Koseki H, Amagai M, and Okada T. Homeostatic pruning and activity of epidermal nerves are dysregulated in barrier-impaired skin during chronic itch development. Sci Rep. **9**: 8625. 2019. [Medline] [CrossRef]
46. Brakkee EM, DeVinney E, Eijkelkamp N, and Coert JH. Sural hypersensitivity after nerve transection depends on anatomical differences in the distal tibial nerve of mice and rats. Ann Anat. **246**: 152038. 2023. [Medline] [CrossRef]
47. Zylka MJ, Rice FL, and Anderson DJ. Topographically distinct epidermal nociceptive circuits revealed by axonal tracers targeted to Mrgprd. Neuron. **45**: 17–25. 2005. [Medline] [CrossRef]